POLITECNICO DI TORINO
Repository ISTITUZIONALE

Development of a frequency-domain model for the aerodynamic flow through volume-averaged porous media

Original
Development of a frequency-domain model for the aerodynamic flow through volume-averaged porous media / Moriaux, O., Zamponi, R., Ragni, D., Avallone, F.. - In: PHYSICAL REVIEW FLUIDS. - ISSN 2469-990X. - 11:(2026). [10.1103/4p9h-fwmv]

Availability:
This version is available at: 11583/3016921 since: 2026-10-23T15:31:13Z

Publisher:
American Physical Society

Published
DOI:10.1103/4p9h-fwmv

Terms of use:

This article is made available under terms and conditions as specified in the corresponding bibliographic description in the repository

Publisher copyright

(Article begins on next page)

18 November 2026

Development of a frequency-domain model for the aerodynamic flow through volume-averaged porous media

Olivier Moriaux [*], Riccardo Zamponi [†], and Daniele Ragni
Department of Flow Physics and Technology, Delft University of Technology, Kluyverweg 1, Delft, 2629HS South Holland, The Netherlands

Francesco Avallone [‡]
Department of Mechanical and Aerospace Engineering, Politecnico di Torino, Corso Duca degli Abruzzi 24, Turin, 10129 Piedmont, Italy

(Received 18 March 2026; accepted 6 October 2026; published 23 October 2026)

The aeroacoustic design of porous trailing-edge inserts for wind turbine noise attenuation requires knowledge of the penetration depth of pressure fluctuations into the porous material. Computationally efficient modeling of the attenuation of unsteady pressure and velocity fluctuations within porous materials will enable improved trailing-edge noise attenuation while minimizing aerodynamic performance loss. Steady models fail to capture the frequency dependence of the attenuation of these fluctuations through the material, while high-fidelity unsteady scale-resolved porous medium models are computationally too expensive for the early-stage design phase. In this study, high-fidelity simulations of a porous material sample subjected to low-amplitude modal inflows are used to evaluate the accuracy of the unsteady Darcy model, which is proposed to fill the gap between high-fidelity unsteady simulations and the steady models for porous medium flows. Two important regimes are identified when considering the local conversion of pressure fluctuations into velocity fluctuations, separated in the frequency domain by a critical frequency. For the investigated porous material and flow conditions, the Strouhal number separating these regimes lies between 0.6 and 1.3, based on the inflow velocity and porous skeleton strut diameter. Above this critical number, pressure and velocity fluctuation attenuation closely follow the unsteady Darcy model. Below this critical number, the local response of the flow features a strong spatial variation throughout the porous sample. In future research, the underlying mechanism affecting the presence of these spatial variations in the low frequencies will be investigated.

DOI: 10.1103/4p9h-fwmv

[*]Contact author: o.k.m.moriaux@tudelft.nl
[†]Also at Department of Environmental and Applied Fluid Dynamics, von Karman Institute for Fluid Dynamics, 1640 Sint-Genesius-Rode, Belgium.
[‡]Also at Department of Flow Physics and Technology, Delft University of Technology, Delft, 2629HS South Holland, The Netherlands.

Published by the American Physical Society under the terms of the Creative Commons Attribution 4.0 International license. Further distribution of this work must maintain attribution to the author(s) and the published article's title, journal citation, and DOI.

I. INTRODUCTION

The dominant aeroacoustic noise source for wind turbines is at the trailing edges of the blades [1]. From the various noise-reduction technologies that have been investigated, permeable trailing-edge inserts have shown the most potential, reducing noise by up to 12 dB [2]. The main mechanism of this noise reduction is the *pressure release mechanism* [2], in which turbulent pressure fluctuations in the boundary layers on either side of the blade section are able to communicate with one another through the permeable trailing edge. Through this communication, the phase difference of these pressure fluctuations is gradually reduced, which decreases their scattering strength at the sharp trailing edge [3].

As noted by Teruna [4], the streamwise length over which communication occurs needs to be long enough compared to the characteristic length of the aerodynamic fluctuations in the boundary layer to allow their phase difference to gradually lessen. Yet, whereas the required streamwise extent of the permeable material decreases with frequency, the attenuation of the fluctuations through the porous material increases too, up to a frequency where communication no longer takes place. Hence, noise reduction may not be achieved in every frequency band, and porous materials need to be designed when targeting the attenuation of a specific noise source. By increasing the permeability parameter of the porous medium, the material becomes less resistive to flow, allowing the pressure release process to occur in higher frequency bands [4].

Considering a homogeneous and isentropic porous material skeleton, an increase in permeability tends to result in a decrease in the shape factor [5]. Hence, the high-inertia mean flow is allowed to penetrate more easily into and through the porous trailing-edge insert [6]. As a result, permeable trailing edges are detrimental to aerodynamic performance [4,7]. First, the equalization of the mean pressure field through the trailing edge lowers lift [4,8]. Second, drag is increased in several ways: (1) the boundary-layer flow sees an increased resistance when penetrating the porous medium [9,10], (2) form drag is increased because the porous medium effectively makes the blade trailing edge partially blunt [3], and (3) the porous material surface results in roughness drag [8]. In addition, at the surface, the interaction of the flow with the porous material results in an increase in high-frequency roughness noise [2]. This surface roughness further increases for materials with larger pore diameters, i.e., materials that generally exhibit high permeability.

For trailing-edge inserts made from a single spatially homogeneous porous material, i.e., *single-layer* inserts, the result is a trade-off between noise reduction over a wide frequency band and aerodynamic performance. Luesutthiviboon *et al.* [6] showed that *multilayer* porous materials can be used to effectively uncouple the permeability and shape factor of the composite porous sample, e.g., by choosing an outer layer with a high shape factor that resists the inertia of the mean flow and an inner layer with a high permeability to promote the communication of low-inertia pressure fluctuations that are able to penetrate through the outer layer. The presented multilayer material prototype served as a promising proof of concept but proved difficult to manufacture and apply in real-world settings due to the fragile construction of the Kevlar layer being stretched over the inner porous material. It is expected that even better aerodynamic and acoustic performance can be extracted from multilayer porous trailing-edge inserts when the material choices and geometric extent of these layers are optimized.

The optimization of such a configuration thus requires a model that is able to capture the penetration depth of unsteady pressure fluctuations into the multiple permeable layers. High-fidelity unsteady simulations consider the volume-averaged Navier-Stokes (VANS) equations [11] to simulate all turbulent scales above the filter length in the equivalent porous medium [12–14]. This modeling approach is analogous to large-eddy simulations (LES) and is therefore computationally too expensive for optimization approaches. Conversely, lower-order models, such as that of Darcy [15], do not consider unsteady flow and therefore cannot model the attenuation of unsteady pressure fluctuations at different length scales. An unsteady Darcy (uD) model [16–20] can be derived from simplifying the VANS equations, which provides a computationally inexpensive method for estimating this unsteady flow attenuation. Yet little research appears to investigate the accuracy of

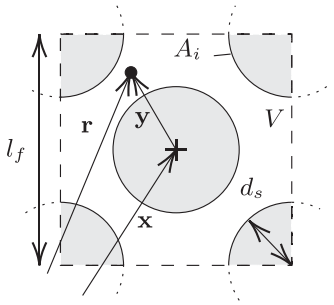


FIG. 1. Diagram of averaging volume V in a structured porous material. The solid phase is indicated in gray and the fluid phase in white. Based on the diagram of Breugem [13, p. 61].

this model in estimating the attenuation of pressure fluctuations through an air-saturated porous sample under flow conditions approaching those inside porous trailing edges.

Such lower-fidelity unsteady volume-averaged models are particularly useful during the early-stage design phase of porous materials for noise attenuation in a wide range of applications, provided that they are able to sufficiently capture the physics that affect the flow penetration needed to model the pressure release process and the penetration of the high-inertia boundary-layer flow into the porous material. Hence, this study aims to clarify the physical relationship between the wavelength of the incoming fluctuation and its attenuation through an air-saturated porous medium, and evaluate the accuracy of the uD model in estimating this attenuation. Such knowledge is pivotal in reducing the full VANS equations to a simpler set of governing equations that can be used for this optimization. This accurate modeling and the gained understanding of the frequency-dependent attenuation of pressure fluctuations will enable porous trailing-edge material designs to target a wider frequency band within which noise is attenuated.

In Sec. II the theoretical framework that matters to the discussion in this paper is briefly explained. The various aspects that comprise the high-fidelity numerical simulations used for this physical investigation are detailed in Sec. III. The data from these simulations are analyzed and discussed in Sec. IV. Finally, the principal findings of this research are summarized in Sec. V.

II. THEORY

When the length scales of interest in the flow are larger than the pore diameter of the material, it is unnecessary to consider its full geometrical description when simulating the flow through it. Hence, our approach uses an equivalent volume-averaged medium representation of the material. The same holds for the aforementioned low-fidelity unsteady porous medium flow models. First, the theory of volume averaging is briefly summarized in Sec. II A. The Darcy-Forchheimer model is a popular closure model for the resistive force of the porous volume-averaged medium on the flow passing through it. By adding only a single unsteady term to this model, i.e., by considering a simplified VANS, a model can be obtained that realistically represents the physics of the frequency-dependent resistance of the porous medium to pressure fluctuations through it [16–18]. This uD model is outlined in Sec. II B.

A. Volume-averaging theory

Volume-averaging theory (VAT) is used to consider the larger-scale effects of the porous material on the flow without needing to resolve scales on the order of the permeable material pore and below. This is achieved by convolving the governing equations of the flow with an averaging window. The concept of the averaging window is illustrated in Fig. 1.

The *superficial* volume average $\langle\cdot\rangle^s$ of fluid quantity ψ_β is defined as

$$\langle\psi_\beta\rangle^s = \int_V \gamma_{\beta\sigma}(\boldsymbol{r})\, m(\boldsymbol{r}-\boldsymbol{x})\, \psi_\beta(\boldsymbol{r})\, \mathrm{d}V. \tag{1}$$

Here $\gamma_{\beta\sigma}$ is a switch function that equals zero within solid regions falling within the porous skeleton structure and equals one when the considered point falls within the fluid (see Fig. 1). In essence, this quantity ensures that the integral is taken over the fluid volume within the integral volume. The filtering function m used to convolve ψ_β needs to integrate to unity over the averaging volume. For structured porous material skeletons, as is the case in this research, a rectangular averaging volume is recommended (see Fig. 1) [13]. The filter length l_f should be large enough to capture the statistical average of the (unstructured) porous material; hence, for structured materials, the filter length should be at least as large as the repeated geometric pattern.

Along with a *superficial* average $\langle\cdot\rangle^s$, an *intrinsic* average $\langle\cdot\rangle$ is defined. These are related to each other through the porosity ε of the porous medium:

$$\langle\psi_\beta\rangle = \varepsilon\langle\psi_\beta\rangle^s. \tag{2}$$

The result is an equivalent fluid medium with a locally increased resistance to flow that models the effect the porous skeleton would have. Therefore, this porous medium no longer contains any geometry that requires a fine mesh to resolve.

B. The Darcy model

In the VANS equations, the spatial scales above the filter cutoff are simulated, and those below may be modeled. However, an additional model is required for the resistive force imposed by the porous material skeleton on the flow passing through it. Commonly, the Darcy-Forchheimer model is considered [11].

In its simplest form, the Darcy model estimates the pressure drop over a given porous material sample thickness that is needed to sustain the volumetric flow rate of fluid passing through a porous medium due to the viscous resistance on the flow. Later, additional corrective terms were added that account for other effects of porous-medium flow to extend the validity of the empirical relation. For example, the Forchheimer corrective term adds a quadratic term to model the inertial resistance on the flow:

$$-\frac{\partial p}{\partial x} = au + bu^2, \quad \text{with } a = \frac{\mu}{K}, \quad b = \frac{\rho c_\mathrm{F}}{\sqrt{K}}. \tag{3}$$

The terms on the right-hand side of Eq. (3) are the Darcy and Forchheimer terms. The porous material permeability is K, and its Forchheimer coefficient is c_F. The fluid viscosity and density are μ and ρ, respectively. The flow velocity u is a superficial volume-averaged one. In other notations, the Darcian flow velocity v_d can be found in its place, which is the volumetric flow rate over the cross-sectional area of the flow.

The model above can be used on its own for steady, spatially homogeneous flows through permeable materials, as there are no time or spatial derivatives of the flow velocity. Otherwise, this model can be incorporated into a range of momentum equations, the simplest of which adds only a time derivative to the model [16–18,21,22]. This model will be referred to as the uDF equation and reads

$$-a^{-1}\frac{\partial p}{\partial x} = u + \gamma u^2 + \tau\frac{\partial u}{\partial t}. \tag{4}$$

All coefficients are normalized by a in the above equation. With the Navier-Stokes equations in mind, this simplified unsteady model makes several assumptions, including the spatial homogeneity of the flow. Yet the resulting analytical relation describes how effectively pressure fluctuations *locally* result in flow velocity.

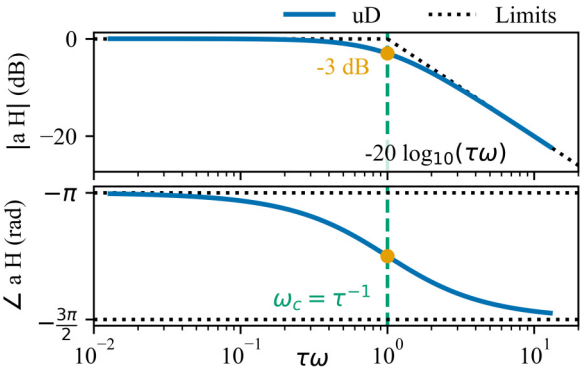


FIG. 2. Frequency response of the normalized uD equations [Eq. (7)].

The uD equation has previously been studied by, among others, Zhu [23]. The frequency response H of the uD equation is defined as

$$\mathrm{H}(s) = U(s)/P(s). \tag{5}$$

The analytic solution for H is derived using the Laplace transform $\mathcal{L}[\cdot]$:

$$\mathrm{H}(s) = \frac{-a^{-1} + \tau u(0) P(s)^{-1}}{\tau s + 1}. \tag{6}$$

For an initial condition of $u(0) = 0\,\mathrm{ms}^{-1}$, this further reduces to

$$\mathrm{H}(s) = \frac{-a^{-1}}{\tau s + 1}. \tag{7}$$

Here U and P are the Laplace transforms of $u(t)$ and $\partial_x p(t)$, respectively. The initial fluid velocity is denoted by $u(0)$. The time constant τ represents the response time of a system to a step function. Several formulations for this parameter were proposed in the aforementioned study. However, for the two most accurate estimates, the parameter is calibrated based on high-fidelity simulations, or it is empirically determined, e.g., with a virtual mass description [23]:

$$\tau = \frac{K\rho}{\mu\varepsilon}\left(1 + C_{\mathrm{vm}}\frac{1-\varepsilon}{\varepsilon}\right), \tag{8}$$

where C_{vm} is the empirically determined virtual-mass coefficient. The time constant depends on the fluid density and the effective viscosity of the porous material, i.e., its permeability. The virtual mass appears to model the added resistance imposed by the porous skeleton on the time response of the system.

An electric analogy can be made to a series RL circuit, where the resistance equals a, the inductance equals τa, the voltage source equals the pressure gradient, and the current equals the fluid velocity. Hence, the time constant τ may be thought of as an inertia that resists change in current, i.e., the fluid velocity. The frequency response H represents how efficiently a frequency component of a voltage fluctuation is converted into a current fluctuation or, equivalently, how efficient a pressure gradient fluctuation results in a flow velocity fluctuation. Such a frequency response is shown in Fig. 2. The frequency response per frequency is decomposed into its amplitude |H| and phase delay ∠H. The amplitude represents how efficiently the amplitude of the source fluctuation, e.g., voltage, is converted into the amplitude of the resultant fluctuation, e.g., current. Whereas the phase delay represents the time lag between the input and output waves. The frequency response of a series RL circuit is known to be a low-pass filter (see Fig. 2). In other words, pressure fluctuations

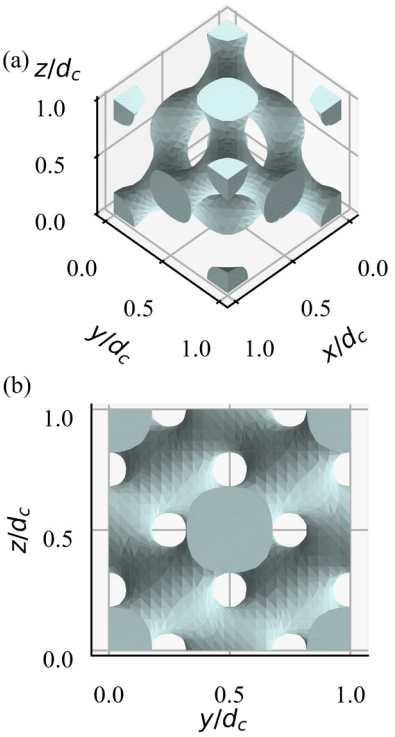


FIG. 3. REV of the altD porous material with a cell size d_c of 2 mm. (a) Isometric view. (b) yz-plane view.

smaller than a critical wavelength experience increased damping. The low-frequency amplitude and high-frequency amplitude slope are both proportional to the porous medium permeability.

III. METHODOLOGY

To investigate the attenuation and phase-delay response of porous materials to an unsteady inflow, high-fidelity simulations are performed. The chosen porous material analyzed in this research is detailed in Sec. III A. The flow configuration is explained in Sec. III B. The CFD solver and the data postprocessing are provided in Secs. III C and III D, respectively.

A. Porous material sample

A single porous material type is tested to limit the scope, allowing the focus to be on characterizing in detail the response of that porous material type to parameters linked to the unsteady inflow. The chosen porous material geometry is the alternate diamond (altD) of the triply periodic minimal surface (TPMS) family, whose shape is parametrically defined as explained in Appendix A [24]. The alternate diamond consists of a 45 ° rotation of the original diamond geometry, as used in previous research of Hunter *et al.* [25]. A representative elementary volume (REV) of the porous material geometry is shown in Fig. 3. This is the smallest possible volume to still statistically capture the geometry, e.g., to converge to the true local porosity of the material. For such structured porous materials, it is the elementary volume that is tiled to form the complete material sample. The chosen REV edge length d_c in this investigation is 2 mm.

The altD is selected for its higher tortuosity compared to the primitive TPMS, which is expected to decrease the size of the region impacted by the entrance effects of the flow into the porous medium. This potentially enables the porous sample thickness to be smaller compared to lower

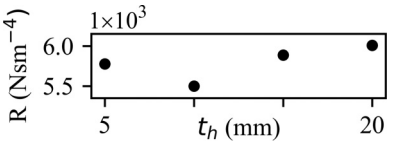


FIG. 4. Porous medium static air-flow resistivity R from the experimental calibration data of a DMND porous material with a cell size d_c of 2.5 mm [28].

tortuosity materials. Also, the altD more closely resembles the DMND porous material analyzed in a previous experimental campaign [26], for which both pressure drop and wind tunnel data are publicly available [5].

The streamwise length of the porous sample is based on the sample thickness t_h needed for the pressure drop Δp through a DMND material with $d_c = 2.5$ mm to converge. The static air-flow resistivity R starts to flatten out near $t_h = 20$ mm in Fig. 4, which is related to Δp according to

$$R = \Delta p/(t_h v_d). \tag{9}$$

Hence, the sample thickness is chosen to also be 20 mm, which ensures that there should be a sufficiently large region inside the porous sample not impacted by entrance effects [27], and therefore more representative of a porous-medium flow in the absence of any additional effects.

B. Permeability test rig simulation setup

A permeability test rig [7] with an unsteady inflow is chosen to analyze the frequency response of the porous material (see Fig. 5). This removes the impact of several flow mechanisms from the analysis, allowing the focus to be on the response of the porous sample to the unsteady inflow. The mean flow follows a single path without any complex interaction of a grazing turbulent boundary-layer flow over the porous surface. Both of these aspects reduce the complexity of the problem, making it more manageable to model. Within a region of the porous sample where the flow is spatially homogeneous, the model equations can be defined for a single repeatable *elementary volume* of the porous medium.

The origin of the reference frame is positioned in the center of the porous sample with dimensions of 20 mm × 8 mm × 8 mm $\{x, y, z\}$. The simulation domain has a length of 24 m and a cross section equal to that of the porous sample.

The light gray regions in Fig. 5 are *sponge* regions that feature increased numerical viscosity. The diagonally dashed regions feature a numerical viscosity that increases exponentially from the center of the domain outward. The regions surrounding this exponential-viscosity zone have constant numerical viscosity values equal to those at the interface with the exponential regions. For example, the outer *sponge* regions, shown in solid gray, have a high constant numerical viscosity. The purpose of the increasing numerical viscosity away from the porous sample is to dampen reflections. More precisely, given the lengths of these high-viscosity regions, the frequency components of the reflection above a critical frequency of 0.2 kHz are dampened. This critical frequency is below the lowest analyzed inflow oscillation frequency to limit the impact of the reflections on the estimated frequency response of the porous material.

The cross-sectional areas of both the simulation domain and the porous material sample are 8 mm × 8 mm. The boundaries along the y and z axes are periodic to limit their impact on the flow inside the porous medium by (1) not producing a boundary layer and (2) not limiting the deflection of the mean flow by the porous sample. The size of the cross section is chosen to be large enough to limit the error caused by having periodic boundaries too close together, which would limit the largest scales in the cross-flow axes. Larger simulation domain cross sections would increase computational cost.

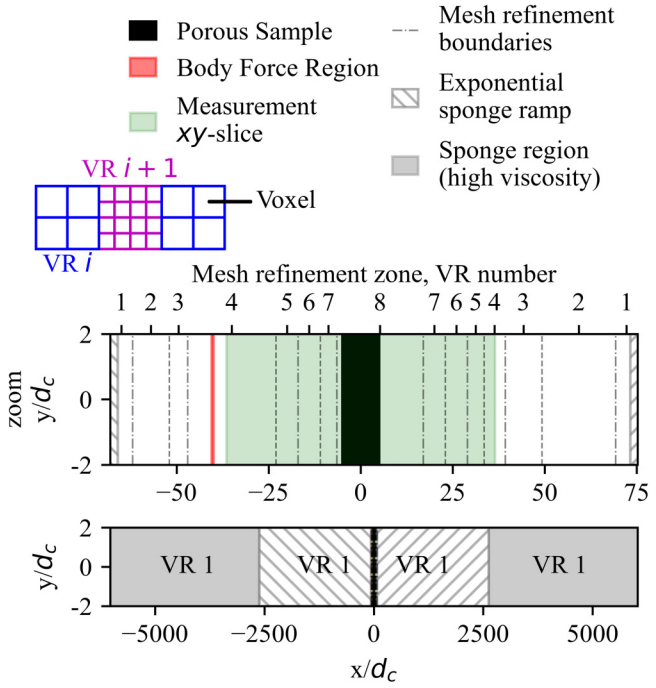


FIG. 5. Simulation domain diagram. The upper figure is a detail of the lower figure, focused on the region around the sample. The limits of the lower figure indicate the simulation domain. The variable resolution (VR) region indices i are provided and explained in the mesh diagram. The local voxel size is $l_{\text{voxel},i} = d_c/2^{i-2}$.

On the outlet, a static pressure boundary condition is defined and set to 101 325 Pa. At the inlet, an unsteady total pressure $p_{0,\text{inlet}}(t)$ is generated. For reasons of parametrization of the signal, repeatability, and implementation in the numerical simulation setup, this signal is defined as

$$p_{0,\text{inlet}}(t) = \Theta + \Psi \sin(2\pi f_p t), \tag{10}$$

where Θ is the mean pressure, Ψ is the amplitude of the oscillating pressure, and f_p is the frequency of the pressure oscillation. This parametrization is based on the work of Zhu [23].

The steady component of the inflow pressure is generated at the inlet surface. The oscillatory component of the inflow pressure field is generated by the body-force region. The reason for splitting the mean and oscillatory parts of the inflow pressure generation is the presence of the *sponge* regions close to the inlet of the simulation domain. In addition to attenuating the reflections, these would also dampen the imposed pressure fluctuations. Hence, the body-force region is positioned between the inlet *sponge* region and the porous sample. The body-force region acceleration Ψ_{bf} is related to the desired oscillatory pressure Ψ following

$$\Psi_{bf} = \Psi/(\rho_0\, l_{bf}), \tag{11}$$

with $\rho_0 = 1.225\,\text{kg}\,\text{m}^{-3}$ being the reference fluid density and $l_{bf} = 1\,\text{mm}$ being the chosen length of the body-force region. This relation couples the force per area of pressure to the acceleration per volume of the body-force region.

C. Numerical simulations

The numerical simulations are performed with 3DS PowerFLOW version 6-2025-R2 [29]. This software uses the Lattice-Boltzmann Method (LBM) to solve for the governing equations considered

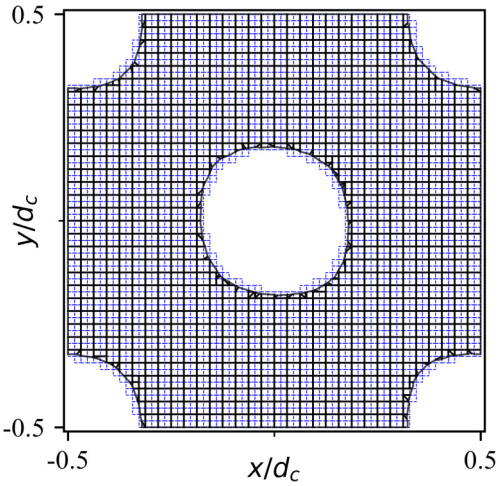


FIG. 6. Detail of the mesh for a single REV, showing a slice on the xy plane at $z/d_c = 0$. The thin blue dashed lines indicate the voxel mesh, and the thick black solid lines indicate the xy-slice measurement file mesh at half the resolution of the volume mesh.

in the very large-eddy simulations (VLES) modeling approach [4]. The simulations use the renormalization group (RNG) $k - \varepsilon$ turbulence model with a wall model that includes pressure gradient effects [29,30], as implemented by PowerFLOW. The chosen model is for low Mach number flows and considers an ideal gas model. As a result, the reported kinematic viscosity and temperature are constant throughout the fluid domain. The inclusion of the turbulence model in the simulations over a "direct" simulation approach enables the simulation time to remain feasible. The mesh around the porous sample has a characteristic spacing approximately twice the Kolmogorov length scale estimated from the local Reynolds number [31]. However, because the simulations employ VLES with the RNG $k - \varepsilon$ model, the smallest turbulent scales are modeled rather than explicitly resolved. The turbulence model does not produce nonphysical attenuation of turbulent fluctuations as the eddy viscosity remains below 3.99×10^{-6} m^2 s^{-1} in the porous sample. In addition, a maximum y^+_{wall} of 1.34 ensures that the reliance on the wall model is minimal. Previous research has successfully used PowerFLOW to reproduce the flow through porous material samples [32], and over porous or serrated trailing-edge inserts [3,33].

Changes in mesh cell size are indicated by the vertical pairs of dashed and dash-dotted black lines in Fig. 5. The mesh is a trimmed mesh; therefore, cell sizes are either doubled or halved at these locations, as illustrated in Fig. 5. In other words, each refinement zone i follows a voxel size $l_{\text{voxel}} = d_c/(2^{n_i})$, with $n_i \in [-1, 6]$, i.e., the number of cells per REV varies 64^3 in the region around the porous sample (see the voxel mesh in Fig. 6) to 0.5^3 in the far field. This coarsest mesh refinement level spans most of the computational domain, ending after the exponential *sponge* region near the inlet and starting again before the exponential *sponge* region near the outlet.

The chosen mesh resolution is validated with a mesh convergence study, which is shown in Fig. 7. The mean pressure drop through the porous sample serves as a metric for the convergence study. Given the total pressure inlet, it is expected that both the mass flow rate and pressure drop will change with the refinement of the mesh. The former is expected to vary with the pressure drop through the simulation domain because total pressure is defined at the inlet. The latter changes due to the more accurate simulation of flow structures in the porous sample at finer voxel sizes. But in addition, for the coarsest mesh, the voxel boundaries may not fully converge towards the defined surface geometry of the porous skeleton. With coarser voxels, the porosity of the material may not accurately represent that of the material one wishes to model.

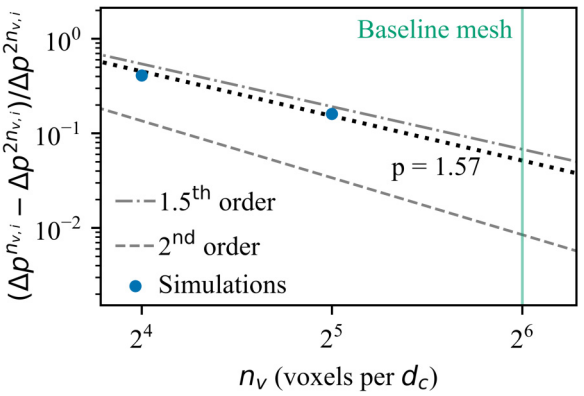


FIG. 7. Mesh convergence study based on steady flow simulations at mesh refinement levels around the porous sample, showing the relative error with respect to the solution of the next-level finer mesh 2 $n_{v,i}$. The pressure drop over the porous sample is computed from two probe points situated at $x/d_c = \{-34, 34\}$ on the center axis with respect to the y and z axes. The fitted convergence rate p is compared to a 1.5th- and second-order convergence rate.

Two cases with locally coarser meshes around the porous sample and in its near wake are investigated, due to a finer-meshed case ($n_v = 2^7$) being computationally too expensive. Applying a Richardson extrapolation method on the data shows a near 1.5th-order convergence rate p for the pressure drop. The convergence rate of PowerFLOW LBM is expected to lie between 2 [34] and 1.5, depending on the influence of the wall boundary condition scheme on the overall convergence rate for the specific case [35].

Estimating a convergence rate for the local TF in the probe points, as investigated in Sec. IV B 2, proves more challenging. Convergence rates show spatial variations across the porous sample due to small differences in the turbulent structures among the mesh resolution levels. In particular, the turbulent structures in the latter half of the porous sample are sensitive to small changes in the upstream structures induced by mesh refinement. As such, the TFs do not converge consistently at all probe locations. Nevertheless, convergence is more consistently observed away from these strongly vortical regions. An example for a single probe outside such regions is provided in Table I, where the relative error ϵ_{rel} of metric y at the mesh refinement level $n_{v,i}$ is defined as

$$\epsilon_{\text{rel}}[\, y^{n_{v,i}} \,] = \left(y^{n_{v,i}} - y^{2\,n_{v,i}}\right) \Big/ y^{2\,n_{v,i}}. \tag{12}$$

The configurations that were simulated with this simulation setup are presented in Table II. The steady cases serve for the mesh convergence study presented in Fig. 7. The aim with the chosen oscillation frequencies was to have two cases below the uD cutoff frequency and two cases above it (see Fig. 2). The cutoff frequency was estimated using the properties of the DMND porous material with a cell size of $d_c = 2.5$ mm (see Fig. 4) [36], which was expected to have similar porous medium

TABLE I. Mesh convergence rate based on the relative error ϵ_{rel} of the local transfer function at $(x/L, y/L) = (-3.50, 0.75)$. The relative error of the base mesh is extrapolated based on the convergence rate of 2.29 and 1.35 for the amplitude and phase, respectively.

Relative error, ϵ_{rel}	$\epsilon_{\text{rel}}[\lvert a\text{TF}\rvert]$	$\epsilon_{\text{rel}}[\angle a\text{TF}]$
Quarter-res.	8.30×10^{-1}	2.48×10^{-1}
Half-res.	1.45×10^{-1}	8.90×10^{-2}
Base (extrapolated)	3.23×10^{-2}	3.67×10^{-2}

TABLE II. Test matrix of the simulations that were performed in this investigation. The columns indicate the inflow oscillation frequency f_p in kHz, whereas the rows indicate the mesh resolution level, i.e., base mesh voxels per $d_c \times \{1, 1/2, 1/4\}$.

Mesh | f_p (kHz)	0	0.3	0.5	1	4	9
Base	×	×	×	×	×	×
Half-res.	×					
Quarter-res.	×					

properties due to the similar appearance of its porous skeleton and similar cell size. For $K = 3.03 \times 10^{-9}$ m^2, $\varepsilon = 0.617$, and a virtual-mass constant in the range of 0.5 to 2 [23], the estimate cutoff frequency would lie between 0.21 kHz and 0.37 kHz. Similarly, with the desired porosity of 0.75 for the TPMS, the estimate cutoff frequency would lie between 0.35 kHz and 0.5 kHz. The additional simulation at 0.5 kHz is performed to see how well the attenuation tracks with the surrounding frequency cases.

D. Data processing

Several data fields are extracted at several probing locations in the simulation domain. The majority of the presented results are based on data taken on an xy slice in the z midspan of the simulation domain, which uses a data sampling frequency of $14 f_p$, which is selected to be much lower than the simulation frequency to limit storage space constraints. Similarly, the data from the slice are exported on a half-resolution mesh, i.e., each measurement cell averages the values of four voxels from the simulation, as shown in Fig. 6.

The measurement file mesh is superimposed on a time instant of the vorticity along the z axis in Fig. 8. This indicates that the vortical structures are resolved on a fine enough mesh. In addition, all contour plots presented in this paper are discrete, i.e., noninterpolated. As such, the edges of the contour cells reflect the measurement file mesh.

VAT allows the large flow structures in the porous medium to be analyzed while averaging out small turbulent structures on scales smaller than the filtering length l_f. Therefore, some of the presented data from the fully resolved porous skeleton LBM simulations are volume averaged to show the large-scale impact of the porous medium on the flow going through it, in the absence of local changes in the flow due to the porous skeleton. Volume-averaged fields are indicated by the intrinsic $\langle\cdot\rangle$ and superficial $\langle\cdot\rangle^s$ averaging operators, as defined by Breugem [13].

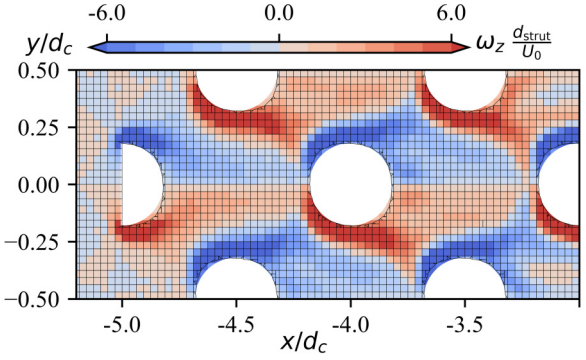


FIG. 8. Time instant of vorticity with the "half resolution" xy-slice measurement file mesh.

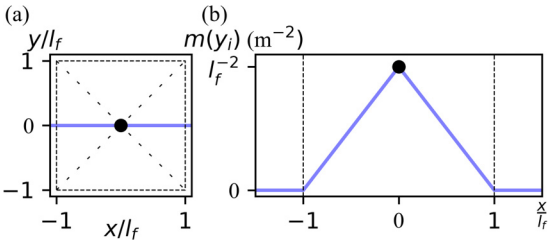


FIG. 9. Cellular filter kernel used for volume averaging [13]. (a) A simple contour of the 2D kernel ($n_{\mathrm{dim}} = 2$). (b) A 1D slice of the 2D contour along $y/d_c = 0$. The dashed line indicates the transition to the zero value, the dot is the location of the filter maximum, the long dashes show the ridges of the pyramid shape, and the solid line indicates the 1D slice in the contour plot.

For the volume-averaging of this ordered porous skeleton, a cellular filter is used with $l_f = 2\,\mathrm{mm}$ (see Fig. 9) [37]. With n_{dim} being the number of axes, this filter is defined by [13]

$$m(\mathbf{y}) = \begin{cases} \prod_{i=1}^{n_{\mathrm{dim}}} (l_{f,i} - |y_i|)/l_{f,i}^2, & \text{for } |y_i| \leqslant l_{f,i} \\ 0 & \text{otherwise} \end{cases}. \tag{13}$$

In other words, for the volume-averaged fields presented here, this filter has a pyramid shape because the data are sampled on the xy slice midplane. The volume-averaged results compare better to existing widespread models that are based on this framework.

The frequency response of the porous material, estimated from the simulation data, is provided as a local *transfer function* TF between the local pressure gradient and the local velocity, both along the x axis. The estimate is computed using the following method [38]:

$$a\mathrm{TF} = \frac{\mu}{K} S\left(-\frac{\partial p}{\partial x}, u_x\right) \Big/ S\left(-\frac{\partial p}{\partial x}, -\frac{\partial p}{\partial x}\right), \tag{14}$$

where $S(x, y)$ is the cross power spectral density between the signals x and y, estimated using Welch's method. In the frequency response contour plots, the response is computed for each data point. The amplitude and phase are then interpolated at the inflow oscillation frequency using the Scipy `PchipInterpolator` function [39]. Finally, the phase is wrapped to a range of 0 rad to -2π rad.

IV. RESULTS

Presented in this section is the analysis of the high-fidelity simulation data of oscillating flow through a porous sample for changing inflow conditions. To understand the impact of *all* unsteady inflow parameters on the response of the porous medium and on the flow through the porous medium, a very large number of simulations would need to be performed, even for the simple offset oscillation in Eq. (10). To retain a feasible scope, the focus of this investigation is placed on the oscillation frequency, as it is perceived to be the main parameter that describes *unsteadiness* according to the uD model in Sec. II B.

The aim of the presented results is threefold. First, we investigate the impact of the inflow oscillation frequency on mean flow through the porous material and on its unsteady flow metrics, as presented in Sec. IV A. Second, we illustrate that pressure and velocity fluctuations flowing through porous media are attenuated by differing amounts based on their wavelength, and that this attenuation cannot therefore be captured by a steady Darcy model and permeability only. This aspect is discussed in Sec. IV B 1. Lastly, we compare the uD model for the frequency response of the porous sample against the high-fidelity simulations in Sec. IV B 2.

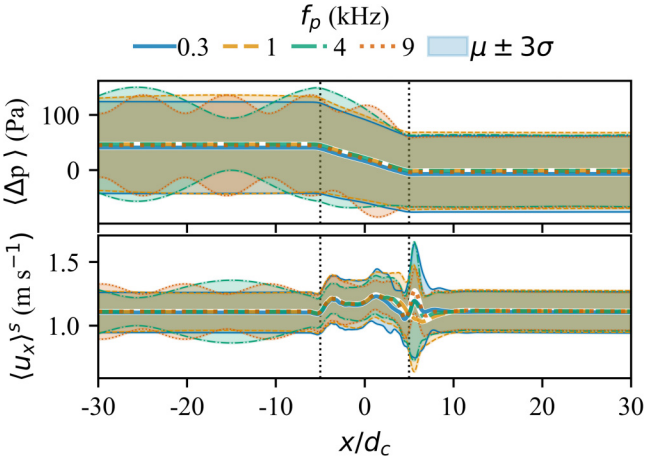


FIG. 10. Spatial evolution of the volume-averaged static pressure and x-axis velocity along the x axis on the xy plane of the LBM simulation performed with different oscillation frequencies f_p. The local mean (lines) and signal bands (filled areas) of each case are shown in the same color. The signal bands are formed by three standard deviations around the mean, i.e., $\mu \pm 3\sigma$. The vertical dotted black lines indicate the spatial extent of the porous material sample. The gauge pressure is defined with respect to the atmospheric outlet pressure.

A. Flow response to inflow oscillation frequency

1. Mean flow

The time average μ and standard deviation bands $\pm 3\sigma$ of the volume-averaged gauge pressure and streamwise velocity through the porous sample are shown in Fig. 10 for all different oscillation frequencies. This figure shows the streamwise evolution of these fields by averaging over the y axis of data acquired on the xy-slice measurement plane (see Fig. 5). Looking at the time average of the flow fields, they appear almost unchanged for all oscillation frequencies, and the pressure gradient over the porous sample is mostly constant.

The flow fields are plotted for only the streamwise extent of the porous sample in Fig. 11. Shown in this figure are the streamwise evolution of the gradient of the static pressure and the *local* Darcy-equivalent permeability estimate in the porous medium, which is computed using the following modification of Eq. (3):

$$K_{\text{est}} = -\mu \langle u_x \rangle^s / \partial \langle p \rangle / \partial x. \tag{15}$$

The turbulent kinetic energy is estimated from the velocity field minus its time average prior to the volume averaging:

$$k = \frac{1}{2}\left(u_x'^2 + u_y'^2 + u_z'^2\right). \tag{16}$$

The mostly constant pressure gradient confirms the possibility of using a linear equation to model the pressure drop caused by the resistance that the material imposes on the flow through it, i.e., the Darcy equation without the Forchheimer correction.

Two different data processing methods are used to estimate the permeability of the porous material using the time-averaged flow. First, the permeability is estimated using the conventional method, which considers the pressure drop Δp over the entire sample thickness t and fits it to the Hazen-Dupuit relation (with $C = 0$):

$$\frac{\Delta p}{t} = \frac{\mu}{K} v_d + \rho C v_d^2, \tag{17}$$

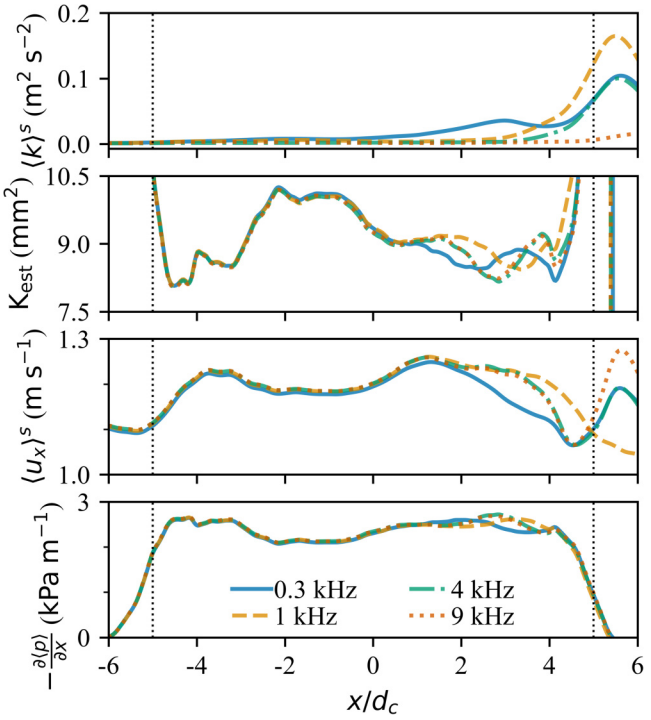


FIG. 11. Streamwise evolution of mean volume-averaged flow turbulent kinetic energy k, velocity, pressure gradient, and estimated local Darcy-equivalent permeability $u_x\mu/(-\partial_x p)$. The vertical black dotted lines indicate the start and end of the porous material.

where C is the form coefficient and v_d is the Darcian velocity. The latter is the volumetric flow rate over the cross-sectional area, replaced in the computations by the superficially averaged streamwise velocity. Second, the local permeability is calculated following Eq. (15) and probed at $x/d_c = 3.5$ in Fig. 11. The estimated permeability derived from both methods is shown in Table III.

The pressure drop estimate for the different frequencies is approximately constant across all frequencies, except for the $f_p = 1$ kHz. The locally probed estimate shows larger variance depending on where the sample is probed, as can also be seen in Fig. 11. From $x/d_c = 0.5$ onward, the permeability estimates start to diverge between the different oscillation frequency cases. This divergence is further discussed in Sec. IV A 2.

As indicated above, the mean flow and the derived Darcy-equivalent permeability of the porous medium appear largely unaffected by the oscillation frequency of inflow pressure fluctuations. In contrast, the bands defined by the oscillation standard deviations change for each case in Fig. 10. In

TABLE III. Permeability estimates of the porous sample [mm^2], based on the mean of volume-averaged xy-slice data. Estimate method (i) *drop* considers the mean pressure drop between points at $x/d_c = -30$ and 30 ($y/d_c = z/d_c = 0$) and the mean volumetric flow-rate averaged over the entire xy slice and the (ii) *local* estimate is similar to the gradient type except for taking the local value at $x/d_c = 3.5$ (see Fig. 11).

K (mm^2)	0.3 kHz	0.5 kHz	1 kHz	4 kHz	9 kHz
Drop	8.39	8.30	8.48	8.38	8.37
Local	8.75	9.10	8.36	8.77	8.85

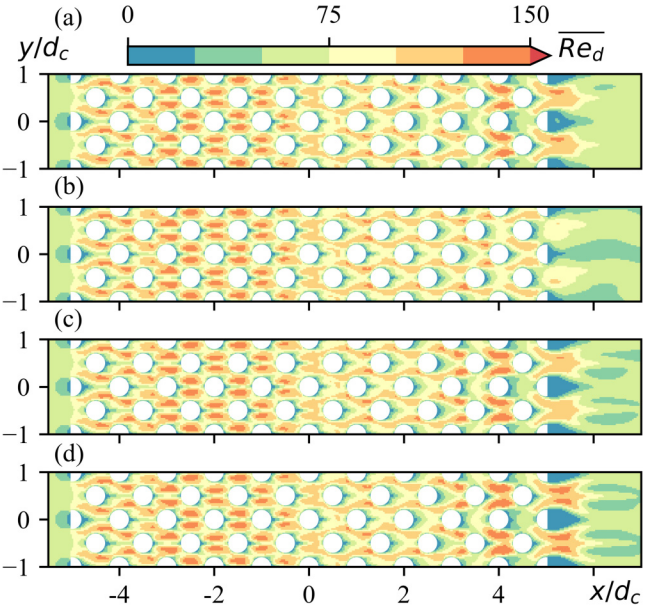


FIG. 12. Contours of the mean local of the strut-based Reynolds number $\overline{\mathrm{Re}_d}$. The presented cases are: (a) $f_p = 0.3\,\mathrm{kHz}$, (b) $f_p = 1\,\mathrm{kHz}$, (c) $f_p = 4\,\mathrm{kHz}$, and (d) $f_p = 9\,\mathrm{kHz}$. The vertical extent of the contour is limited to $y/d_c \in [-1, 1]$ for clarity.

large part, this is caused by a standing wave pattern due to the reflection of the incoming pressure fluctuation wave against the front and back surfaces of the porous sample. The outflow region behind the sample shows a constant and similar oscillation amplitude for all cases, indicating that the wave transmitted into the porous sample is likely to also have a similar amplitude across all oscillation frequency cases. In other words, the oscillations at different frequencies can be considered to be superimposed on the frequency-invariant mean flow field. As such, the choice is made to consider the linear uD model [see Eq. (7)] to represent the unsteady flow response through the porous medium instead of the nonlinear unsteady Darcy-Forchheimer (uDF) model (see Appendix B).

2. Flow structure

While the mean flow shows little variance with oscillation frequency, it does indicate a consistent streamwise variation of the flow through the porous sample in Fig. 11. The flow structures inside the porous material may impact the frequency response of the sample. Therefore, to investigate these flow structures, the mean and variance of the local strut-diameter-based Reynolds number for several simulation cases are shown in Figs. 12 and 13, respectively.

The mean flow structure inside the porous sample shows no dependence on oscillation frequency (see Fig. 12); it is a result of the porous sample geometry and the mean flow. Vortex shedding around an array of staggered 3D struts is complex and does not appear to be thoroughly described. For example, a lot of research on flow through arrays of cylinders considers periodic streamwise boundary conditions [13,40,41], meaning that the vortical structures are spatially converged. This is very useful when analyzing the physics of a spatially invariant flow, but it does not fully reflect the flow in a real porous sample with a finite thickness. Research that does consider a unidirectional and nonperiodic inflow through an array of cylinders [42] shows a similar streamwise evolution of vortex shedding in the cylinder array as shed vortices interact with one another and impinge on downstream cylinders. As such, even though the inflow conditions may dictate steady and symmetric

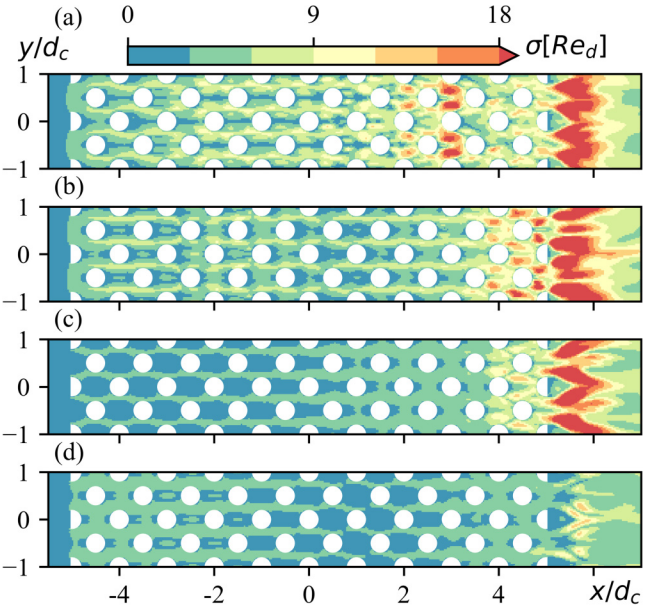


FIG. 13. Contours of the local standard deviation of the strut-based Reynolds number $\sigma[\mathrm{Re}_d]$. The presented cases are (a) $f_p = 0.3$ kHz, (b) $f_p = 1$ kHz, (c) $f_p = 4$ kHz, and (d) $f_p = 9$ kHz.

vortex shedding around a singular cylinder ($\mathrm{Re}_d \approx 40$) [43, p. 2], in an array the vortices will grow increasingly unsteady and asymmetric, as is the case in Fig. 12.

When the fluid enters the sample, it flows around the porous skeleton struts in an ordered and steady manner, i.e., this flow structure remains unchanged over time. The steady flow is likely caused by the strong local pressure gradient pushing the flow into the porous material (see Fig. 11). After approximately $x/d_c = -3.5$, symmetric vortex structures form behind the struts. This is similar to cylinder Stokes flow and is accompanied by a drop in the local pressure gradient in Fig. 11.

From $x/d_c = 0.5$ onward, the vortices become increasingly asymmetric, similar to higher Reynolds number cylinder flow. As mentioned above, the more turbulent vortex shedding is caused by the interaction of shed vortices from the different struts and the impingement of upstream vortices on the downstream struts. The pressure gradient also slowly recovers to its original larger and constant value. The streamwise volume-averaged evolution of k in Fig. 11 shows a small and gradual growth after the energetic entrance region. A transition to a much larger and more noticeable growth in k occurs between $x/d_c \in [0.5, 2.5]$ for most oscillation-frequency cases.

Finally, before exiting the porous sample, the local Reynolds number of the flow slightly increases. The spatial extent of these structures in the porous sample appears unaffected by the oscillation frequency, as is evident from Fig. 12. All cases show a strong increase in k in this outflow region in Fig. 11.

Adding an oscillation to the mean flow affects the time-variance of the flow (see Fig. 13). Most research on flow through arrays of cylinders [41,44] considers oscillating flow with a zero mean, i.e., not unidirectional. Following the prior assumption that the flow behaves quite linearly, the findings of the aforementioned research will be used to contextualize the presented flow. Three parameters are highlighted by Etminan *et al.* [41]: the inflow Reynolds number, the density of the cylinders, i.e., the inverse of the porosity, and the Keulegan-Carpenter number (KC):

$$\mathrm{KC} = U_{\mathrm{ref}}\, T/d_{\mathrm{cyl}} = U_{\mathrm{ref}}/(f_p\, d_{\mathrm{strut}}). \tag{18}$$

The reference velocity U_{ref} is the oscillation amplitude, T is the period of the oscillation, and d_{cyl} is the diameter of the cylinders, i.e., the struts in this case.

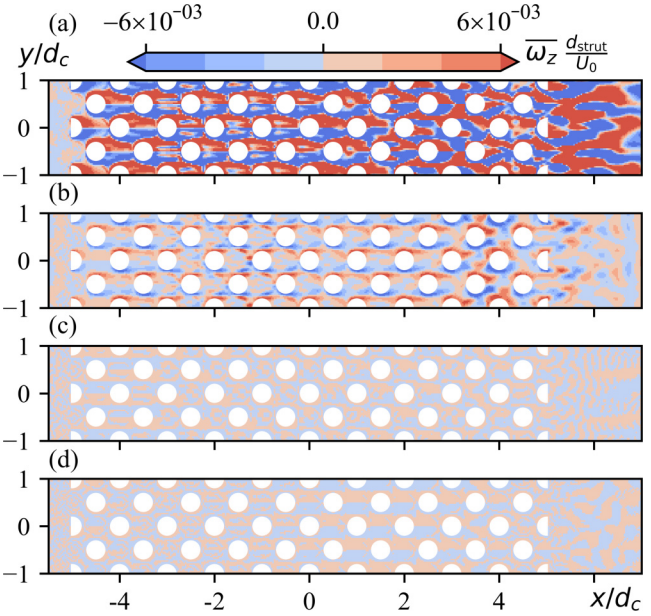


FIG. 14. Contours of the mean band-passed normalized vorticity around the z-axis $\omega_z\, d_{\text{strut}}/U_0$. The presented cases are (a) $f_p = 0.3\,\text{kHz}$, (b) $f_p = 1\,\text{kHz}$, (c) $f_p = 4\,\text{kHz}$, and (d) $f_p = 9\,\text{kHz}$. Each case is band passed in a frequency band of $f_p \pm 50\,\text{Hz}$.

For the unidirectional oscillating flow, vortex shedding is not simply based on the oscillation amplitude, as the steady flow velocity logically contributes to the vortex shedding, similarly to steady flow vortex shedding. Hence, for the purpose of this analysis, the mean flow velocity is taken as it represents the order of magnitude that flows around the cylinders, i.e., $U_{\text{ref}} = 1.1\,\text{ms}^{-1}$. For the strut diameter of 0.7 mm, the KC numbers associated with the four main oscillation frequencies are 5.2, 1.6, 0.39 , and 0.17. For such a low Reynolds number, no separation of the flow from the cylinders should occur for KC $\lesssim 2$. Separation should start to occur with increasing KC, up to KC $= 7$. The lower two frequency cases fall within or close to this range where vortices start to separate from the cylinders. Whereas for the higher two oscillation frequency cases, the flow around that oscillation frequency should remain attached to the cylinders. This difference means that for the cases where the vortices detach, they are able to interact with each other and impinge on downstream struts, leading to a strong increase in flow velocity variance towards the downstream part of the porous material for the low-frequency cases in Fig. 13.

The vorticity computed from the band-passed flow around each oscillation frequency can be visualized to confirm the above mentioned behavior of vortical structures formed by unsteady flow around these oscillation frequencies (see Fig. 14).

These results confirm that only the lower frequencies have detached vortices, which then spatially evolve due to their interaction with other vortices and struts.

The changed flow structure after $x/d_c = 0.5$, that can be observed for the two lower-frequency cases in Figs. 13 and 14, also appears to coincide with the streamwise location from which onward larger spreads are observed between the mean flow of the simulation cases in Fig. 11. A hypothesis is that this different flow in the downstream section of the porous material is sensitive to the turbulence generated by the upstream part of the sample. Similarly, the 1 kHz case shows a different flow in the downstream section of the sample with respect to the other cases in Fig. 12. This discrepancy in shedding behind the sample shows up even though all four simulations use similar simulation periods, with similar settling times after their steady-flow initialization. This different shedding

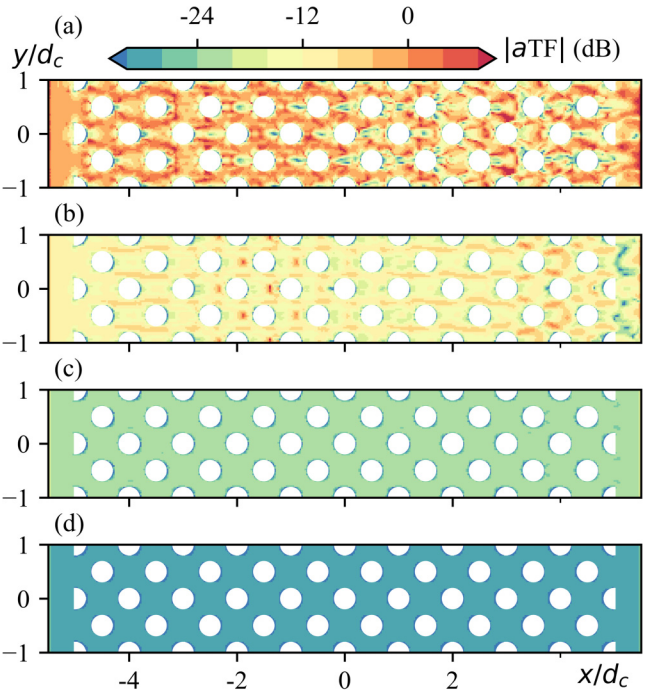


FIG. 15. Contours of the normalized local TF amplitude for inflow pressure oscillation frequencies of (a) 0.3 kHz, (b) 1 kHz, (c) 4 kHz, and (d) 9 kHz.

behind the porous sample likely affects the resistance of the porous sample, resulting in a different estimate of the permeability compared to the other frequency cases in Table III.

B. Porous material frequency response

The analysis of the flow structure inside the porous medium showed only frequency dependence in the deviations of the flow fields with respect to their mean. The mean flow itself did not show a clear inflow-frequency dependence. Yet, for the porous sample to behave according to the uD model, the frequency response estimated from the high-fidelity simulation data should show a noticeable change with inflow oscillation frequency.

The frequency response can be analyzed in two ways. First, contour plots show the spatial variation in attenuation and phase delay for a single inflow oscillation frequency in Sec. IV B 1. Second, for a number of points of interest in the material, the local response can be plotted as a function of inflow oscillation frequency, e.g., Fig. 2. The latter also enables the simulated response to be compared to the uD equation, which only shows the frequency dependence as it assumes spatial homogeneity. The probed frequency response is analyzed in Sec. IV B 2.

1. Spatial variation of the porous medium response

The frequency response as defined by the uD model is a local property describing the conversion of a pressure gradient fluctuation to a velocity fluctuation. In other words, the frequency response of the material is similar to the dynamic permeability described by Johnson *et al.* [20]. The local frequency response, or TF as defined in Eq. (14), is shown for each oscillation frequency case in Fig. 15. Only the TF *amplitude* is included as it is expected to most clearly indicate whether the porous medium follows a similar frequency-dependent behavior of the uD model.

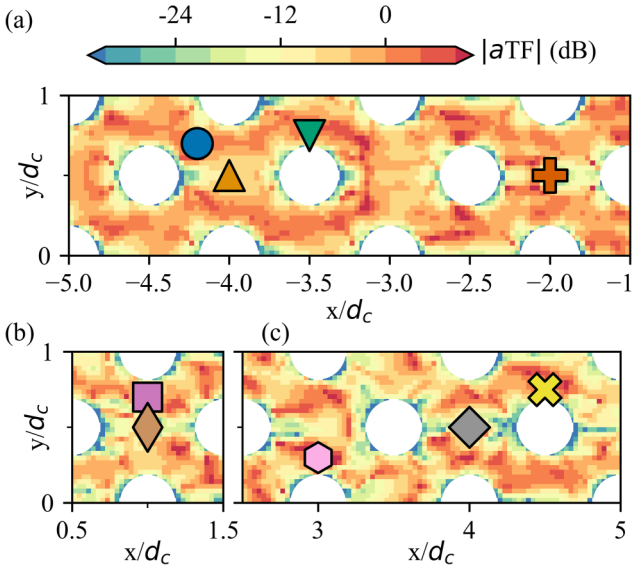


FIG. 16. Contours of normalized local TF amplitude for the case of $f_p = 0.3\,\text{kHz}$. The markers indicate the positions of the probed frequency responses plotted in Fig. 17. Shown are the TF contours for different streamwise locations: (a) $x/d_c \in [-5, -1]$, (b) $x/d_c \in [0.5, 1.5]$, and (c) $x/d_c \in [2.5, 5]$.

Several aspects can be remarked from Fig. 15. First, the overall frequency response amplitude level decreases with inflow oscillation frequency. Hence, the overall porous sample attenuation of pressure fluctuations increases with frequency, similar to the uD model. How closely the attenuation is estimated by the uD model will be described in Sec. IV B 2. Second, the lowest-frequency case ($f_p = 0.3\,\text{kHz}$) shows a substantial spatial variation in the frequency response that decreases with increasing frequency. As such, the highest frequency case shows little to no spatial variation. Third, this spatial variation comes in the form of *flow paths* through the porous material sample. With *flow paths*, it is meant that these regions of high $|a\text{TF}|$ are concentrated along paths between the porous material struts and their bound vortices, similar to what one could imagine to be the pathlines of the flow. The shape and streamwise evolution of these flow paths appear similar to the structures shown by the local Reynolds number standard deviation in Fig. 13. Along these flow paths, the conversion from pressure gradient fluctuations to velocity fluctuations is most efficient. The frequency dependence of the attenuation and the flow paths may be better contextualized by the probed frequency response results shown in Sec. IV B 2. Hence, the discussion regarding the presence of these flow paths is continued in the subsequent section.

For the second analysis method, the points of interest of where to probe the porous sample for comparison against the uD model need to be determined. As shown previously, the local frequency response varies strongly with probe location. A pair of probes is positioned near $x/d_c = -4$ to represent the inflow into the sample, one probe in the middle of the pore in the wake of a strut and the other in the *flow path*. The probe at $x/d_c = -3.5$ serves to analyze the flow where symmetric vortices start to form behind the struts. The probes from $x/d_c = -2$ to $x/d_c = 3$ are positioned throughout the region where the flow slowly transitions to an increasingly unsteady shedding. Lastly, the response at the outflow of the sample is analyzed with probes around $x/d_c = 4$. The probe locations are visualized in Fig. 16.

2. Frequency dependence of the porous medium response

The response of the material in these probe points as a function of inflow oscillation frequency is shown in Fig. 17. Note that, since this porous medium *system* is likely nonlinear, thus this frequency

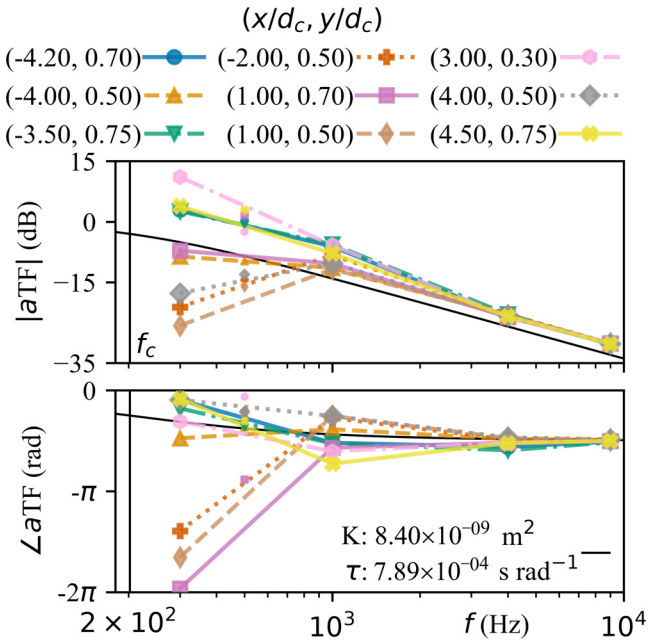


FIG. 17. Attenuation and phase-delay of four simulations at differing inflow oscillation frequencies, estimated at different streamwise locations x/d_c along the porous sample. The thin black line represents the frequency-domain solution to the uD equation using the permeability estimate of the *drop* method in Table III and the associated cutoff frequency. The model parameter values are provided in the figure. An additional simulation case at $f_c = 0.5$ kHz is provided as a reference but not included in the frequency response lines.

response cannot be generalized for any input. In other words, the presented attenuation and delay results are responses of separate systems. Exciting the system simultaneously with all four pressure oscillation frequencies may not result in a linear combination of the four responses. Still, these results are plotted together as they indicate different *regimes* of the porous sample when excited by a low-amplitude aerodynamic oscillation.

Comparing the probed frequency responses to the theoretical response, the uD model is able to reasonably predict the frequency-dependent attenuation and phase delay (see Fig. 17). The model parameter τ used for the model fit is selected to be at the limit of the range provided by Zhu [23, p. 26] from Lowe *et al.* [22], i.e., $\tau \in [7.89 \times 10^{-4}\,\mathrm{s\,rad^{-1}}, 1.05 \times 10^{-3}\,\mathrm{s\,rad^{-1}}]$ as based on the virtual-mass coefficient C_{vm} range [see Eq. (8)]. The small constant offset between the model and data in the amplitude of the frequency response is likely due to a small inaccuracy in the permeability estimate from the mean-flow pressure drop data (see Table III). Also, the phase matches the model trend quite closely.

Two additional aspects can be noted in the amplitude of the frequency response plot in Fig. 17, which are related to the discussion that was started in Sec. IV B 1. First, the attenuation and phase delay estimated for each frequency case start to spread out more based on probing location when going towards the lower frequencies, i.e., for 1 kHz and lower. Second, the low-frequency case pairs (0.3 kHz and 1 kHz) show shallower slopes of attenuation to frequency than the high-frequency case pairs.

The first aspect regarding spatial variance of the local frequency response emphasizes the frequency dependence of the spatial variance observed in Fig. 16. It is hypothesized that this is likely due to the strong influence of local flow conditions and the porous material geometry at larger scales. Much like with the energy cascade of other turbulent flows, turbulence is produced at a length scale based on the large-scale flow geometry, i.e., the porous skeleton struts in this

case [13,31]. These large-scale vortical structures break apart into increasingly small scales until they are effectively dissipated by viscous effects. At these much smaller length scales, the viscous effects dominate over other flow effects, such as inertia.

The critical frequency separating both of these regimes differs from the uD model critical frequency f_c that is proportional to τ^{-1}. Observing the increased spatial variance towards the lower frequencies, the critical frequency describing the onset of spatial variance towards the lower frequencies appears to be situated between 1 and 2 kHz. Considering the local flow velocity in each probe point and the porous skeleton strut diameter, this equated to a Strouhal number between 0.6 and 1.3.

The second aspect of the two regimes of attenuation-to-frequency slope is directly indicative of the change in dominant mechanisms affecting the propagation of fluctuations through the porous sample. Considering the uD equation, the effective behavior of the porous material is that of a low-pass filter, where pressure fluctuations below a critical length scale become rapidly attenuated. At larger length scales, however, the viscous attenuation is not as effective, and the slope flattens. The equivalent critical frequency f_c, i.e., the cutoff frequency related to the viscous Darcy term, is inversely proportional to the model parameter τ, as described in Fig. 2.

The higher-frequency oscillation cases are very well described by the Darcy term, whose role is to represent these viscous losses caused by the porous skeleton interacting with the flow. As noted by Breugem [13], pressure and velocity fluctuations in porous-wall channel flows decay exponentially with their depth in the porous medium, and this affects smaller-scale fluctuations more strongly. More crucially, the exponentially decaying amplitude of the frequency response at high frequencies indicates that the conversion of pressure fluctuations into velocity fluctuations becomes increasingly inefficient. The lack of energetic flow paths that efficiently transfer energy deep into the porous sample at the higher oscillation frequencies is the likely cause for the decreasing strength and spatial extent of the high local Reynolds number standard deviation regions in the downstream segment of the porous sample in Fig. 13.

Conversely, above a certain critical length scale, the viscous effects are not the dominant mechanism. For these low-frequency cases, the amplitude of the local frequency response shows clear communication paths through the porous material where pressure fluctuations are effortlessly converted to velocity fluctuations, which do not appear to be present for the high-frequency cases in Fig. 15. The presence of these flow paths results in a strongly probe-location-dependent frequency response. The four probes located behind the skeleton struts, i.e., $y/d_c = 0.5$, consistently show the lowest values of $|a\mathrm{TF}|$ in the low frequencies in Fig. 17. All higher-amplification probes are located within the *flow paths* at varying streamwise locations. With streamwise location, the shape of these flow paths and their local amplitude change. This may be related to the changing vortical shedding structures behind the struts, which are affected by the shedding of the upstream structures, as shown in Fig. 14.

The question remains about what physical mechanism relates to the presence of the communication paths and whether a critical length-scale can be found to predict within which behavioral frequency band a fluctuation will fall. Some candidates for scaling can be considered. First, the porous skeleton strut diameter: this length scale could be linked to the *natural*, i.e., steady-inflow, shedding frequency of vortices behind the struts through a certain Strouhal number. Oscillation frequencies above the natural shedding frequency of the material structure would pass through without altering the shed vortices, while lower frequency oscillations might strongly affect these natural vortices. However, while the flow velocity is very low, so are the strut diameter and the Strouhal number associated with cylinder vortex shedding around $\mathrm{Re}_d = 50$, i.e., St between 0.1 to 0.18 [45,46]. Observing the power spectral densities of the flow data in the TF probe points, a small peak around $\mathrm{St} = 0.1$ ($f_p \in [0.18\,\mathrm{kHz},\ 0.32\,\mathrm{kHz}]$) can be seen for the cases where the inflow oscillation frequency does not overlap with this presumed shedding frequency. This peak falls below the forced oscillation frequency in the 1 kHz case where the spatial variation is still clearly present, as shown in Fig. 18. Therefore, the natural vortex shedding hypothesis is considered not to be the fluid mechanism affecting the spatial variance in TFs.

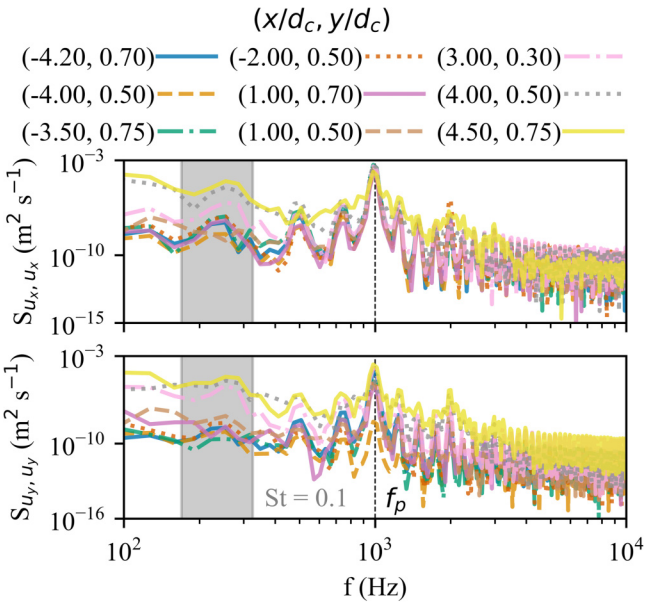


FIG. 18. Power spectral density S_{u_i,u_i} of the flow velocity components in the probe points of Fig. 17 for the inflow oscillation case $f_p = 1$ kHz. The natural shedding frequency band of the porous struts is estimated based on the local flow magnitude in the probe point and St = 0.1.

Alternatively, with the strut diameter, a parallel to rapid distortion theory can be drawn [47]. Small turbulent scales would be deformed by the struts, whereas large eddies would be partially blocked but otherwise unaffected. The repeated deformation from subsequent struts may lead to stronger mixing of the turbulence, diffusing the energy faster and leading to no communication path.

Second, another candidate for the length scale is that of the square root of permeability $\sqrt{K}$. The reasoning behind this length scale is that the lack of communication paths at high frequencies is caused by the exponential attenuation of fluctuations through a porous material, which is proportional to its permeability. From a certain attenuation onward, the fluctuations may be of such small amplitude (see Fig. 19) that the propagation is close to purely acoustic. The wave diffracts as a whole around all the struts of the porous skeleton instead of communicating along efficient flow paths.

It is clear that the wavelength or frequency of the fluctuation propagating through the porous sample matters greatly when estimating its attenuation through a porous medium, not only in the acoustic regime but also for pressure or velocity fluctuations of a more aerodynamic amplitude. Estimates of the attenuation of fluctuations based only on a steady Darcy fail to account for this strong frequency dependence. The simple uD model presents a valid starting point to estimate the frequency-dependent efficiency of the material in converting weak pressure fluctuations into velocity fluctuations. Because the uD model considers the porous sample as a volume-averaged equivalent medium, it should apply to a wide range of porous materials, irrespective of their porous skeleton type, provided that representative model parameters are used.

In addition, the pore-resolved simulations of the altD material revealed a clear cutoff frequency in the frequency response of the porous material that delimits two regimes for the propagation of fluctuations through the porous sample. In the high-frequency regime, fluctuation amplitudes steeply decay with increasing fluctuation frequency, and fluctuations are not able to fully penetrate through the porous sample. Since the frequency response is accurately described by the unsteady Darcy equation, this regime is dominated by viscous resistance and is therefore expected to occur

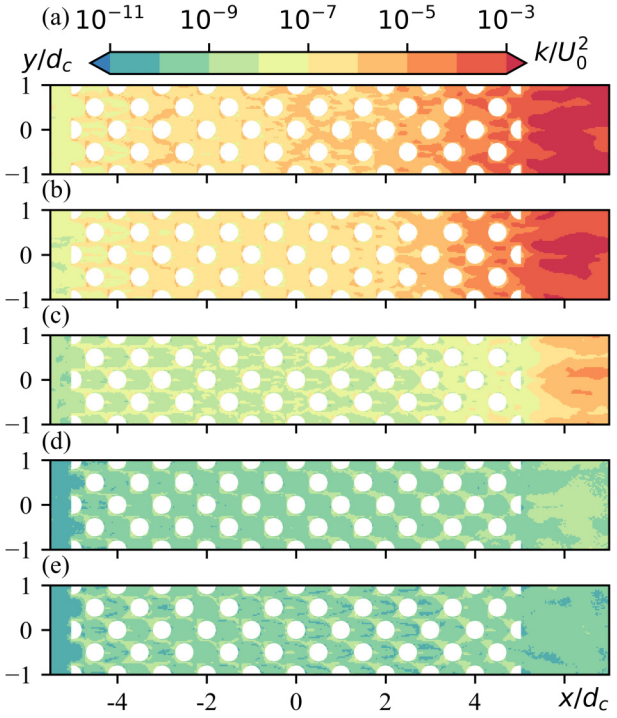


FIG. 19. Contours of the band-passed turbulent kinetic energy k/U_0^2 of the steady-inflow case. The frequency band used for the band-passing is defined as $f_{\text{center}} \pm 50$ Hz, where the f_{center} is (a) 0.2 kHz, (b) 0.3 kHz, (c) 1 kHz, (d) 4 kHz, and (e) 9 kHz.

in other porous materials, i.e., with structured or unstructured geometries. In the low-frequency regime, fluctuations are carried through the porous sample along flow paths formed by the velocity fluctuations around that frequency. In these flow paths, pressure fluctuations most efficiently produce velocity fluctuations, resulting in a high local frequency response and thus a strong spatial variation in local frequency response through the porous sample. The observed cutoff frequency delimiting both regimes appears to differ from the theoretical cutoff frequency f_c of the uD equation, as the physics that affect the low-frequency regime remain important above this theoretical cutoff frequency, up to a Strouhal $\text{St}_d = f d_{\text{strut}}/U_0$ of 0.6 to 1.3. This Strouhal-number range is specific to the altD porous sample and the flow conditions considered here and may shift for other cases. Nevertheless, the results provide further evidence of two frequency regimes in the response of the porous material to fluctuations, consistent with the findings of Zhu and Manhart [18] and Johnson *et al.* [20]. The distinct flow paths associated with the low-frequency regime of the frequency response may therefore depend on the structured geometry of the altD porous material and may hence be less evident in unstructured porous materials.

The gained insight into the propagation of aerodynamic fluctuations through the porous sample is of great interest, as to achieve noise attenuation for porous trailing-edge inserts, these pressure fluctuations need to be able to reach through the insert thickness to communicate. Simultaneously, the desire is to limit the flow velocity through the porous material at lower frequencies, where it impacts the mean aerodynamic performance of the airfoil. A model based on the uD equation can be useful in designing a material for such a trade-off, and the volume-averaged nature of the model allows for a wide range of porous materials to be considered. However, observed from these results is the necessity to investigate the strong spatial variation in frequency response in the low frequencies, where preferential flow paths appear. A better understanding of the physics at play in

the low-frequency domain allows the porous material properties to react differently in these low frequencies without potentially increasing attenuation of high-frequency fluctuations. Additional model terms would be needed to longer assume spatial homogeneity in the frequency domain uD model and capture this spatial variance.

V. CONCLUSION

Current methods for evaluating the aerodynamic performance of porous materials in the initial design stages either consider only the steady-state response or are computationally too expensive for the rapid prototyping of the material. The unsteady response of porous media to oscillations of acoustic magnitudes is well understood and modeled. However, for aerodynamic fluctuations that form the source of trailing-edge noise [4], more research is needed on the porous medium frequency response to develop a model for the aeroacoustic optimization of porous materials in the initial design stage.

The results of this research show that the attenuation and phase-delay induced by a porous material on weak aerodynamic pressure waves passing through it varies strongly with the wavelength of said fluctuations. For a low Reynolds number porous medium flow, as shown to occur inside porous trailing-edge inserts in wind turbine blades, the computationally efficient uD model can be used to estimate the wavelength-dependent attenuation and delay that these waves exhibit when passing through a porous material. The nature of such volume-averaged models allows for a large variety of porous material geometries to be considered, given their accurate parametrization.

When using a steady Darcy model to describe the aerodynamic performance of a porous material, the frequency dependence of the attenuation is ignored. This leads to the overestimation of the strength of high-frequency fluctuations deep inside the porous material and, therefore, to a possible overestimation of the frequency band over which a pressure release process would take place for a permeable trailing edge. Using the VANS equations with the Darcy term to model the resistance of the material to the flow, the dynamics of this weakly oscillating aerodynamic flow can be modeled. However, the analytic solution to the uD equation can already be used for the initial design of the porous material response to unsteady inflow at various wavelengths.

In this research, two regimes for the propagation of fluctuations through a porous sample were observed, depending on the frequency of the fluctuation. For a low oscillation frequency, the fluctuations travel along flow paths formed by velocity fluctuations around that frequency. Along these paths, pressure gradient fluctuations are most efficiently converted into velocity fluctuations. From a critical frequency onward, viscosity as described by the Darcy term becomes dominant, i.e., a Strouhal number around 0.6 to 1.3, based on the inflow velocity and porous skeleton strut diameter. With increasing viscous resistance, the velocity fluctuations at the core of the flow paths are attenuated. The lack of such flow paths at high frequencies means there is little to no spatial variance in the local frequency response of the flow. Because this flow domain is also dominated by viscous resistance, the uD equation accurately estimates the frequency response at high oscillation frequencies. Although the volume-averaged uD model also predicts the two frequency regimes, indicating that they do not arise from the specific pore topology, the distinct flow paths observed in the low-frequency regime may depend on the structured nature of the porous material considered in this study.

The flow analyzed in this research is somewhat unique in that it represents flow through an array of cylindrical struts, but is unidirectional and does not consider periodicity in the streamwise direction, as this better represents the flow through a porous trailing edge. Similar to the research of oscillating bidirectional water flows [41], i.e., with a zero mean, a separated vortex can be observed for the lower oscillation frequencies, whereas the higher frequency oscillations appear to have fully attached flows around the cylinders. The separated vortices in the low frequencies interact with each other and impinge on downstream struts, resulting in a streamwise evolution of the vortical structures, which would not be captured if streamwise periodicity were imposed.

To accurately capture the frequency response of a porous sample over the entire frequency domain, it is advised that an additional term be added to the current uD equations to account for the presence of *fluctuation communication paths* in low frequencies, which results in locally more efficient conversion of pressure fluctuations into velocity fluctuations. Understanding the source of this low-frequency propagation of fluctuations would allow for the material to be tuned to attenuate the low- and high-frequency oscillations differently, allowing for noise attenuation through the pressure release process while limiting the penetration of very low frequency oscillations that negatively impact aerodynamic performance. Once such a low-order model for the pressure release process is achieved, the implementation of that frequency-domain model for the porous medium in the simulation of large-scale geometries can be investigated.

ACKNOWLEDGMENTS

This publication is part of the project AMPERE with File No. 20467 of the Open Technology research program, which is (partly) financed by the Dutch Research Council (NWO).

O.M.: conceptualization, methodology, software, validation, formal analysis, investigation, resources, data curation, visualization, writing–original draft.; R.Z.: conceptualization, methodology, writing–review and editing, supervision; D.R.: conceptualization, methodology, writing–review and editing, resources, supervision, project administration, funding acquisition; F.A.: conceptualization, methodology, software, writing–review and editing, supervision.

DATA AVAILABILITY

The data that support the findings of this article are openly available [48].

APPENDIX A: ALTD TPMS

The AltD geometry for the porous material (see Sec. III A) is described by an isosurface of the following equation:

$$\cos\left(\frac{2\pi x}{L_x}\right)\cos\left(\frac{2\pi y}{L_y}\right)\cos\left(\frac{2\pi z}{L_z}\right) - \sin\left(\frac{2\pi x}{L_x}\right)\sin\left(\frac{2\pi y}{L_y}\right)\sin\left(\frac{2\pi z}{L_z}\right) = 0.4264. \quad \text{(A1)}$$

The REV length is defined by $\{L_x, L_y, L_z\}$ in the respective axes. The local coordinate value in REV is given by $\{x, y, z\}$. Tiling together multiple REVs created by this isosurface results in the full porous material sample.

The value of the right-hand side of Eq. (A1) is set to achieve a porosity of 75%. On the 2D xy slice the computed porosity is approximately 83% away from the boundaries with the outer flow.

APPENDIX B: THE DARCY-FORCHHEIMER MODEL

Similarly to the uD model, an uDF model can be defined. When adding the Forchheimer term, the differential equation becomes nonlinear, which complicates solving for an analytic description of the frequency response. Similarly to Eq. (6), the Laplace transform of the uDF equation [see Eq. (4)] is taken, which results in

$$U(s) = \frac{-a^{-1}P(s) + \tau u(0)}{\tau s + 1} - \frac{\gamma}{\tau s + 1}\mathcal{L}[u^2]. \quad \text{(B1)}$$

The first terms on the right-hand side describe the linear part of the differential equation (uD), and the last term describes the nonlinear $N[\cdot]$ Forchheimer part. Using the Adomian Decomposition Method (ADM) [49], the previously determined solution to the linear uD equation can be iteratively corrected for the nonlinear term. This is achieved by describing the solution u, or its Laplacian U,

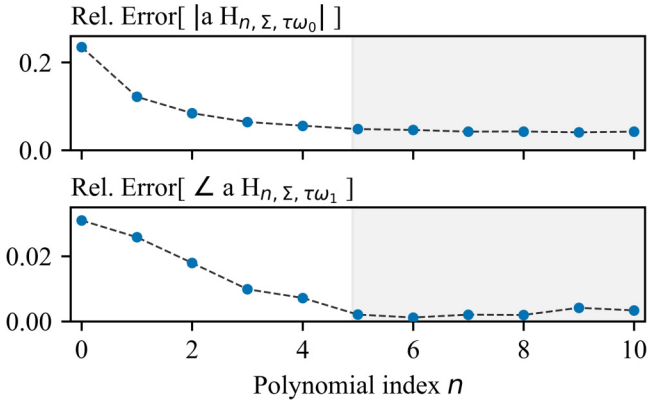


FIG. 21. Convergence of the frequency response H_n [Eq. (5)] with increasing number of corrective terms U_n [Eq. (B6)]. The amplitude is probed at $\tau\omega_0 = 2 \times 10^{-2}$ and the phase is probed at $\tau\omega_1 = 5 \times 10^{-1}$. The response $H_{n,\Sigma}$ is the sum of all terms up to and including term n. The relative error is defined with respect to the mean amplitude and phase values inside the gray-filled region.

and the nonlinear term $\mathcal{L}[u^2]$ with infinite sums:

$$U = \sum_{n=0}^{\infty} U_n, \qquad \mathcal{L}[u^2] = \sum_{n=0}^{\infty} A_n, \tag{B2}$$

where A_n are Adomian polynomials, formally defined as

$$A_n = \frac{1}{n!}\frac{d^n}{d\lambda^n}\left(N\left[\sum_{i=0}^{\infty}\lambda^n u_i\right]\right)_{\lambda=0}. \tag{B3}$$

For the quadratic nonlinear term here, this formulation simplifies to

$$A_0 = u_0^2, \quad A_1 = 2u_1u_0, \quad A_2 = 2u_2u_0 + u_1^2, \ldots. \tag{B4}$$

The resulting sum reads

$$\sum_{n=0}^{\infty} U_n = \frac{-a^{-1}P + \tau u(0)}{\tau s + 1} - \frac{\gamma}{\tau s + 1}\mathcal{L}\left[\sum_{n=0}^{\infty} A_n\right]. \tag{B5}$$

The first component of the solution ($n = 0$) considers only the linear part of the equation, i.e., the uD equation. The remaining components act as the aforementioned corrective terms and can be described by

$$U_n(s) = -\frac{\gamma}{\tau s + 1}\mathcal{L}[A_{n-1}] \quad \text{for } n \in \{1, 2, 3, ...\}. \tag{B6}$$

Through the inverse Laplace transform, each term can be described in the time domain u_i. These terms then form part of the Adomian polynomials for higher-order corrective terms.

Mathematica [50] is used to iteratively derive the desired number of corrective terms [51]. Because each new term is a polynomial combination made from all previous terms, the complexity and computational cost increase quite rapidly. The required number of terms needed for the solution to converge depends on the particular nonlinear equation. The frequency response is probed at the positions where the corrective terms U_n ($n > 0$) are largest and is shown in Fig. 20. A relative error with respect to the mean of the last six cumulative frequency response estimates is shown. This number is chosen because the phase reaches convergence after around five terms. The amplitude retains some limited oscillation around the mean value, which results in a convergence towards

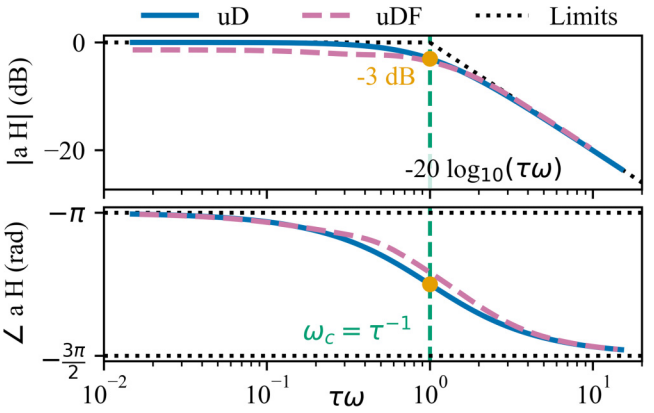


FIG. 22. Frequency response of the normalized uD and uDF equations. The Forchheimer term is estimated with 10 additional Adomian polynomial terms ($n = 10$). The initial velocity $u(0)$ is set to $0\,\mathrm{ms}^{-1}$ [Eq. (B5)].

this constant error. The presented solution in Fig. 21 is considered adequate, considering the high computational cost of computing more terms.

The resulting frequency-response estimate is nonlinear and depends on the input function $\partial_x p(t)$. To limit the complexity, solutions are derived for either a step function $\partial_x p(t) = \Theta$ or a *settled* offset oscillation $\lim_{t\to+\infty} \partial_x p(t) = \Theta + \Psi \sin(\omega_p t)$. The first excites all frequencies, whereas the latter excites only the oscillation frequency. However, the latter inflow condition can be reproduced more accurately in high-fidelity simulations than an ideal step function. The presented frequency-response estimate in Fig. 21 considers a step function as input pressure gradient. For the step-function case, the Forchheimer term affects only the low frequencies, whereas the Darcy term primarily damps the high frequencies (see Fig. 21).

A large disadvantage of the presented uDF solution is that the response is very sensitive to the model parameters, easily resulting in erroneous frequency responses. This is more than likely caused by the quadratic term.

[1] S. Oerlemans, P. Sijtsma, and B. Méndez López, Location and quantification of noise sources on a wind turbine, J. Sound Vib. **299**, 869 (2007).

[2] A. Rubio Carpio, F. Avallone, D. Ragni, M. Snellen, and S. van der Zwaag, Mechanisms of broadband noise generation on metal foam edges, Phys. Fluids **31**, 105110 (2019).

[3] C. Teruna, F. Avallone, D. Ragni, A. Rubio-Carpio, and D. Casalino, Numerical analysis of a 3-D printed porous trailing edge for broadband noise reduction, J. Fluid Mech. **926**, A17 (2021).

[4] C. Teruna, Aerodynamic noise reduction with porous materials: Aeroacoustics investigations and applications, Ph.D. thesis, Technische Universiteit Delft, HS Delft (2022).

[5] O. Moriaux and R. Zamponi, A benchmark dataset for the grazing flow over porous materials (Version 3) [Dataset], Zenodo, 2025, https://doi.org/10.5281/zenodo.15044105.

[6] S. Luesutthiviboon, D. Ragni, F. Avallone, and M. Snellen, An alternative permeable topology design space for trailing-edge noise attenuation, Int. J. Aeroacoust. **20**, 221 (2021).

[7] A. Rubio Carpio, R. Merino Martínez, F. Avallone, D. Ragni, M. Snellen, and S. van der Zwaag, Experimental characterization of the turbulent boundary layer over a porous trailing edge for noise abatement, J. Sound Vib. **443**, 537 (2019).

[8] T. F. Geyer and E. Sarradj, Trailing edge noise of partially porous airfoils, in *20th AIAA/CEAS Aeroacoustics Conference* (American Institute of Aeronautics and Astronautics, Atlanta, GA, 2014), p. 3039.

[9] Y. Kuwata and K. Suga, Extensive investigation of the influence of wall permeability on turbulence, Int. J. Heat Fluid Flow **80**, 108465 (2019).
[10] C. Teruna, F. Manegar, F. Avallone, D. Ragni, D. Casalino, and T. Carolus, Noise reduction mechanisms of an open-cell metal-foam trailing edge, J. Fluid Mech. **898**, A18 (2020).
[11] S. Whitaker, The Forchheimer equation: A theoretical development, Transp. Porous Media **25**, 27 (1996).
[12] B. D. Wood, X. He, and S. V. Apte, Modeling turbulent flows in porous media, Annu. Rev. Fluid Mech. **52**, 171 (2020).
[13] W. P. Breugem, The influence of wall permeability on laminar and turbulent flows: Theory and simulations, Ph.D. Thesis, Delft University of Technology, 2005.
[14] M. Jadidi, A. Revell, and Y. Mahmoudi, Pore-scale large eddy simulation of turbulent flow and heat transfer over porous media, Appl. Therm. Eng. **215**, 118916 (2022).
[15] H. Darcy, *Les Fontaines Publiques De La Ville De Dijon : Exposition Et Application Des Principes a Suivre Et Des Formules a Employer Dans Les Questions De Distribution D'eau; Ouvrage Terminé Par Un Appendice Relatif Aux Fournitures D'eau De Plusieurs Villes Au Filtrage Des Eaux Et A La Fabrication Des Tuyaux De Fonte, De Plomb, De Tole Et De Bitume* (Victor Dalmont, Libraire des Corps imperiaux des ponts et chaussées et des mines, Paris, 1856).
[16] K. R. Hall, G. M. Smith, and D. J. Turcke, Comparison of oscillatory and stationary flow through porous media, Coastal Eng. **24**, 217 (1995).
[17] R. J. Lowe, J. R. Koseff, and S. G. Monismith, Oscillatory flow through submerged canopies: 1. Velocity structure, J. Geophys. Res.: Oceans **110**, 2004JC002788 (2005).
[18] T. Zhu and M. Manhart, Oscillatory Darcy flow in porous media, Transp. Porous Media **111**, 521 (2016).
[19] D. Lasseux, F. J. Valdés-Parada, and F. Bellet, Macroscopic model for unsteady flow in porous media, J. Fluid Mech. **862**, 283 (2019).
[20] D. L. Johnson, J. Koplik, and R. Dashen, Theory of dynamic permeability and tortuosity in fluid-saturated porous media, J. Fluid Mech. **176**, 379 (1987).
[21] Z. Gu and H. Wang, Gravity waves over porous bottoms, Coastal Eng. **15**, 497 (1991).
[22] R. J. Lowe, U. Shavit, J. L. Falter, J. R. Koseff, and S. G. Monismith, Modeling flow in coral communities with and without waves: A synthesis of porous media and canopy flow approaches, Limnol. Oceanogr. **53**, 2668 (2008).
[23] T. Zhu, Unsteady porous-media flows, Ph.D. thesis, Technische Universität München, Munich, 2016.
[24] S. B. G. Blanquer, M. Werner, M. Hannula, S. Sharifi, G. P. R. Lajoinie, D. Eglin, J. Hyttinen, A. A. Poot, and D. W. Grijpma, Surface curvature in triply-periodic minimal surface architectures as a distinct design parameter in preparing advanced tissue engineering scaffolds, Biofabrication **9**, 025001 (2017).
[25] T. P. Hunter, F. Avallone, N. A. K. Doan, and D. Ragni, Aerodynamic characterisation of communicating turbulent boundary layers through a porous medium subjected to a pressure differential, in *30th AIAA/CEAS Aeroacoustics Conference* (American Institute of Aeronautics and Astronautics, Rome, Italy, 2024), p. 3049.
[26] O. K. Moriaux, R. Zamponi, S. Satcunanathan, M. Meinke, and W. Schroeder, Experimental and numerical investigation of the turbulent boundary layer of a grazing flow over porous materials, in *30th AIAA/CEAS Aeroacoustics Conference* (American Institute of Aeronautics and Astronautics, Rome, Italy, 2024), p. 3050.
[27] C. Teruna, L. Rego, F. Avallone, D. Ragni, and D. Casalino, Applications of the multilayer porous medium modeling approach for noise mitigation, J. Aerospace Eng. **34**, 04021074 (2021).
[28] R. Zamponi, F. Avallone, D. Ragni, C. Schram, and S. van der Zwaag, Relevance of quadrupolar sound diffraction on flow-induced noise from porous-coated cylinders, J. Sound Vib. **583**, 118430 (2024).
[29] Dassault Systemes, PowerFLOW 2022 user's guide (2024), https://www.3ds.com/support/documentation/powerflow-2022-product-documentation-and-installation-guides.
[30] ANSYS, Inc., *Fluent 2024 R2: Fluent Theory Guide* (ANSYS, Canonsburg, PA, 2024), Chap. 4.3.2. RNG k-ϵ Model.
[31] S. B. Pope, The scales of turbulent motion, in *Turbulent Flows* (Cambridge University Press, Cambridge, UK, 2000), pp. 182–263.

[32] T. P. Hunter, F. Avallone, N. A. K. Doan, and D. Ragni, Characterization of communicating turbulent grazing flows through a resolved porous medium, Flow, Turbul. Combust. **116**, 10 (2026).
[33] F. Avallone, W. C. P. van der Velden, D. Ragni, and D. Casalino, Noise reduction mechanisms of sawtooth and combed-sawtooth trailing-edge serrations, J. Fluid Mech. **848**, 560 (2018).
[34] Q. Liao, G. Li, J. Li, L. Xue, S. Tian, and X. Song, Convergence analysis of lattice Boltzmann method for Stokes flow in digital rock characterization, Geoenergy Sci. Eng. **230**, 212161 (2023).
[35] K. Hoefnagel, D. Casalino, S. Hulshoff, and F. de Prenter, A second-order volumetric boundary treatment for the lattice Boltzmann method, SSRN (2025).
[36] R. Zamponi, D. Ragni, S. van der Zwaag, and F. Avallone, Innovative coatings for reducing flow-induced cylinder noise by altering the sound diffraction, Phys. Fluids **35**, 127120 (2023).
[37] M. Quintard and S. Whitaker, Transport in ordered and disordered porous media II: Generalized volume averaging, Transp. Porous Media **14**, 179 (1994).
[38] H. Vold, J. Crowley, and G. T. Rocklin, A comparison of H1, H2, Hv frequency response functions, in *Proceedings of the 3rd International Modal Analysis Conference, Orlando, Florida, USA* (Union College, Schenectady, NY, USA, 1985), pp. 272–278.
[39] P. Virtanen, R. Gommers, T. E. Oliphant, M. Haberland, T. Reddy, D. Cournapeau, E. Burovski, P. Peterson, W. Weckesser, J. Bright, S. J. van der Walt, M. Brett, J. Wilson, K. Jarrod Millman, N. Mayorov, A. R. J. Nelson, E. Jones, R. Kern, E. Larson, C. J. Carey, *et al.*, SciPy 1.0: Fundamental algorithms for scientific computing in Python, Nat. Methods **17**, 261 (2020).
[40] J. L. Shearer, Electric network analog study of viscous flow normal to parallel, evenly spaced cylinders, Text. Res. J. **29**, 467 (1959).
[41] V. Etminan, R. J. Lowe, and M. Ghisalberti, Canopy resistance on oscillatory flows, Coastal Eng. **152**, 103502 (2019).
[42] F. He, S. Draper, M. Ghisalberti, H. An, and P. Branson, Predicting mean flow through an array of cylinders, Geophys. Res. Lett. **51**, e2024GL110164 (2024).
[43] B. M. Sumer and J. Fredsøe, *Hydrodynamics Around Cylindrical Structures*, revised ed. (World Scientific, Singapore, 2006).
[44] Y. Zhao and Y. Shi, Characterization of flow separation around inline cylinders within oscillatory flow, Shock Vibration **2018**, 7569432 (2018).
[45] A. A. Roshko, *On the Development of Turbulent Wakes from Vortex Streets*, Technical Note 2913 (California Institute of Technology, Washington, DC, 1952).
[46] H. Jiang and L. Cheng, Strouhal–Reynolds number relationship for flow past a circular cylinder, J. Fluid Mech. **832**, 170 (2017).
[47] R. Zamponi, S. Moreau, and C. Schram, Rapid distortion theory of turbulent flow around a porous cylinder, J. Fluid Mech. **915**, A27 (2021).
[48] O. Moriaux, A numerical dataset for low Reynolds number unidirectional oscillating flow through a porous material, (Version 1) [Dataset], Zenodo, 2026, https://doi.org/10.5281/zenodo.19062948.
[49] L. Mulatu, A. Wilkins, A. Chowdhury, and C. Franklin, A note on solving nonlinear differential equations using modified Laplace decomposition method, IJRDO **5**, 12 (2019).
[50] Wolfram Research, Inc., *Mathematica*, version 14.3 (Champaign, Illinois, 2025).
[51] J.-S. Duan, An efficient algorithm for the multivariable Adomian polynomials, Appl. Math. Comput. **217**, 2456 (2010).